ACS APPLIED MATERIALS & INTERFACES

www.acsami.org

Research Article

Swelling-Assisted Sequential Infiltration Synthesis of Nanoporous ZnO Films with Highly Accessible Pores and Their Sensing Potential for Ethanol

Daniel Pleshek, John Tran, Yuzhe Li, Asghar Shirani, Elena V. Shevchenko,* and Diana Berman*

Cite This: *ACS Appl. Mater. Interfaces* 2021, 13, 35941−35948

Read Online

ACCESS | Metrics & More | Article Recommendations | Supporting Information

ABSTRACT: Here, we report a swelling-assisted sequential infiltration synthesis (SIS) approach for the design of highly porous zinc oxide (ZnO) films by infiltration of block copolymer templates such as polystyrene-*block*-polyvinyl pyridine with inorganic precursors followed by UV ozone-assisted removal of the polymer template. We show that porous ZnO coatings with the thickness in the range between 140 and 420 nm can be obtained using only five cycles of SIS. The pores in ZnO fabricated via swelling-assisted SIS are highly accessible, and up to 98% of pores are available for solvent penetration. The XPS data indicate that the surface of nanoporous ZnO films is terminated with −OH groups. Density functional theory calculations show a lower energy barrier for ethanol-induced release of the oxygen restricted depletion layer in the case of the presence of −OH groups at the ZnO surface, and hence, it can lead to higher sensitivity in sensing of ethanol. We monitored the response of ZnO porous coatings with different thicknesses and porosities to ethanol vapors using combined mass-based and chemiresistive approaches at room temperature and 90 °C. The porous ZnO conformal coatings reveal a promising sensitivity toward detection of ethanol at low temperatures. Our results suggest the excellent potential of the SIS approach for the design of conformal ZnO coatings with controlled porosity, thickness, and composition that can be adapted for sensing applications.

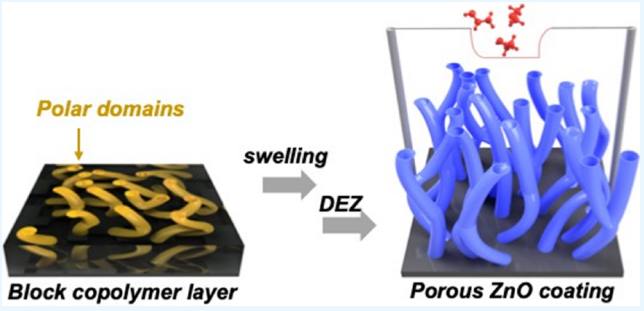

KEYWORDS: *nanoporous zinc oxide, ZnO, sequential infiltration synthesis, quartz crystal microbalance, ethanol sensing, chemiresistivity, block copolymer, low-temperature sensitivity*

1. INTRODUCTION

The urge for clean air, preservation of the environment, and non-invasive diagnostics emphasize the importance of analytical systems capable of selective and sensitive analysis of gases in industrial, residential, and medical settings. Metal oxide semiconductors are widely used as major sensing components for the detection of various gas molecules with good selectivity and fast and high response signals.[1,2] Detection of gases in such sensors is based on the changes in mass or electrical or electrochemical properties of the metal oxide upon coming in contact with the sensed species. The sensing layer based on metal oxide semiconductor materials is usually fabricated in a form of a film. Such films can be deposited either from chemically synthesized nanoparticles via dip coating, sol−gel processing, and hydrothermal synthesis[3,4] or directly by chemical vapor deposition, RF magnetron sputtering, electrospinning, angle deposition, molecular beam epitaxy, metal−organic chemical vapor deposition, or atomic layer deposition (ALD).[5,6] Among other metal oxides, zinc oxide (ZnO) offers very high thermal and chemical stability that makes it one of the most frequently used material systems in gas sensors.[7,8]

However, chemiresistive ZnO-based gas sensors generally require the heating of the sensing layer to a high temperature (200−500 °C), leading to high energy consumption and changes in the nanomaterial microstructure.[9] While despite the long history of the practical application of ZnO for sensing of ethanol, acetone, etc., the mechanism responsible for the change in resistivity in chemiresistive ZnO is still under debate, it is generally accepted that high temperature is needed to displace the chemisorbed molecules of oxygen and oxidize ethanol.[10,11] Multiple efforts have been explored to lower the operating temperature requirements. Among them, doping of ZnO[12] and its interfacing with different materials[13] are the most common approaches. ZnO is also used as a sensing layer in adsorption/absorption mass-based sensors[14] that can

Received: May 4, 2021
Accepted: July 15, 2021
Published: July 23, 2021

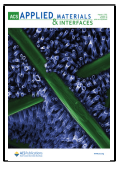

operate at room temperature but is less cost-efficient as compared to chemiresistive sensors.

Improvement in the gas sensing sensitivity is usually associated with high surface area availability. Nanostructured materials with a high surface area characterized by enhanced gas sensing properties[5] and hence fabrication of nanostructured (e.g., nanoporous) conformal coatings are critical for further progress in the design of sensing materials both for chemiresistive[15,16] and mass-based sensors.[17,18] Here, we report that highly porous ZnO uniform conformal coatings with controlled porosity and thickness and uniformity can be synthesized by infiltration of the block copolymer (BCP) matrix via sequential infiltration synthesis (SIS).[19,20] We probe the ethanol sensing capabilities of the resulting films by comparing the quartz crystal microbalance (QCM) adsorption results to the resulting changes in the electrical conductance of the materials at room temperature and 90 °C. Our results demonstrate the high sensitivity of the films to the reducing environment of ethanol, even at low temperatures, thus suggesting the excellent potential of SIS-designed ZnO for sensing applications.

2. EXPERIMENTAL DETAILS

2.1. Polymer Template Preparation. The samples of nanoporous ZnO films with different porosities and thicknesses were synthesized using a swelling-assisted SIS approach. Polystyrene-*block*-polyvinyl pyridine (PS-*b*-P4VP) polymer powders with molar weights 75k-*b*-25k and 25k-*b*-25k were purchased from Polymer Source Inc. The powders were dissolved in toluene at a concentration of 3 wt %. The resulting polymer solutions were filtered through 0.4 and 0.2 μm sized filters to remove residual large agglomerates. Polymer solutions were spin-coated on silicon dioxide wafers (300 nm thick SiO_2 on Si, 10 mm square samples) or AT-cut QCM crystals (1 in. in diameter with resonant frequency ∼5 MHz, purchased from Fil-Tech) with SiO_2-coated electrodes. A silicon dioxide substrate was used to eliminate surface contribution to conductivity, while ZnO enabled better adhesion of the coatings. Spin-coating of the polymers was performed at 2000, 3000, and 4000 rpm that resulted in coating thicknesses of 330, 260, and 150 nm for 25−25 and 420, 280, and 140 nm for 75−25 BCPs, correspondingly.

2.2. Swelling-Assisted SIS. Swelling of the polymers before the SIS process was performed to enable better full-thickness diffusion of the inorganic vapors and to introduce additional functional groups for the infiltration.[21] Swelling was performed in ethanol, being selective to polar vinyl pyridine domains of the BCP, at 75 °C for 1 h.[22] After 1 h, the samples were carefully removed from ethanol and dried at room temperature in a fume hood for at least 2−3 h. The drying step was performed at room temperature to prevent the collapse of the swelling-introduced porosity in the polymers.

2.3. Vapor-Phase Infiltration. Infiltration of ZnO in the polymer was performed using SIS in an ALD system (Cambridge ALD system). The recipe for the infiltration was adapted from the previously reported aluminum oxide infiltration with the trimethylaluminum precursor being replaced by diethyl zinc (DEZ). The samples were placed on a stainless steel tray inside the ALD chamber at 90 °C to avoid melting of swelling-formed predefined polymer structures. Nitrogen flow (100 sccm) was introduced into the chamber for 30 min prior to the infiltration. Five cycles of the ZnO infiltration were performed as follows: the DEZ precursor was introduced at 10 mTorr with 20 sccm nitrogen flow into the reactor for 400 s; after the predetermined time, when the infiltration of the polymer occured, the excess reactant was evacuated followed by introduction of H_2O at 10 mTorr for 120 s; the chamber was then purged with nitrogen at 100 sccm to remove non-infiltrated byproducts. The bulk ZnO coating had been deposited directly on the silicon dioxide substrate without the polymer template and using 500 cycles of the regular ALD process.[23]

2.4. Polymer Removal. After the infiltration, the polymer templates were removed by exposing the infiltrated samples to ultraviolet (UV) ozone (UVOCST16 × 16 OES, 254 nm UV wavelength) for 10 h. Previously, this procedure was shown to be effective for polymer removal without the need to overheat the QCM substrates and thus to prevent their loss of sensitivity. The porosity of the resulting samples had been measured with spectroscopic ellipsometry to be 50% and 70% for PS25-*b*-P4VP25 and PS75-*b*-P4VP25 correspondingly similarly as in previous studies with SIS-synthesized nanoporous alumina.[24]

2.5. QCM Analysis. The QCM technique was used for the quantitative analysis of the materials infiltration process as well as for sensing characterization. The changes in the resonant frequency and mechanical resistance of the QCM oscillations were monitored using a SRS QCM200 controller. For the analysis of infiltration steps, the readings of the QCM resonant frequency were stabilized for at least 1 h at room temperature (22 °C) in the ambient environment before recording the measurements. In sensing tests, the QCM setup was placed in a custom-built vacuum chamber connected to nitrogen gas and ethanol supply. The chamber also allows heating from the room temperature up to 90 °C. In the chamber, two samples, one deposited on the QCM and one deposited on the silicon dioxide substrate prepared using exactly the same sample preparation procedure, were connected next to each other for simultaneous absorption and electrical conductivity measurements. Electrical conductivity measurements were performed using the van der Pauw method with four probes connected to the corners of the sample and resistance measured using a 2401 Keithley Source Meter. The QCM sample had been fixed in a custom-designed stainless steel holder connected to heating elements and a thermocouple for the controlled temperature tests. To remove the effect of air and disruptive moisture on the ZnO samples, after inserting the QCM and wafer sample in the vacuum chamber, the chamber was pumped down ∼10^{-3} Torr. Then, the samples were exposed to the ethanol vapors introduced to the chamber at a rate of ∼3 Torr/min until the pressure in the chamber reaches 4 Torr (monitored using a 275 Granville-Phillips Vacuum Gauge). The absorption capacity of the QCM samples was calculated based on the change in the QCM resonant frequency that is directly proportional to the added mass:[25−27]

$$\Delta f = -\frac{2f^2}{A\sqrt{\rho_q \mu_q}}\Delta m \quad (1)$$

where f is the frequency of oscillation of the unloaded crystal, ρ_q is the density of quartz (2.648 g cm^{-3}), μ_q is the shear modulus of quartz (2.947 × 10^{11} g cm^{-1} S^{-2}), A is the QCM surface area, and Δm is the mass change.

Changes in the electrical conductivity of the sample deposited on the silicon dioxide wafer and in the QCM resonance frequency of the sample deposited on the QCM substrate were performed simultaneously for direct correlation. All of the measurements were repeated at least three times upon introducing the ethanol vapors and evacuating the chamber. A similar analysis has been performed using water, acetone, and toluene vapors.

2.6. Characterization. Scanning electron microscopy (SEM) analysis was performed using a FEI Nova SEM. Transmission electron microscopy (TEM) analysis on the samples crushed and deposited on a carbon mesh TEM grid was performed using a JEOL 2100F microscope. Chemical modifications of the polymer templates during swelling and infiltration were evaluated using a Nicolet 6700 Fourier transform infrared spectrometer (FTIR) with a 700−4000 cm^{-1} spectral range. X-ray diffraction (XRD) analysis was performed using a Bruker D2 XRD with Cu Kα source of irradiation.

2.7. Density Functional Theory Calculations. The density functional theory (DFT) calculations were performed using the framework of DFT in the Vienna Ab initio Software Package (VASP 5.4.1). The simulation models of ZnO surfaces, with and without hydroxide groups, and ethanol molecules were built using Material Studio. For this, a 2 × 2 ZnO supercell included five layers in the (111) plane and one layer of O−H groups or O atoms was added on

https://doi.org/10.1021/acsami.1c08225
ACS Appl. Mater. Interfaces 2021, 13, 35941−35948

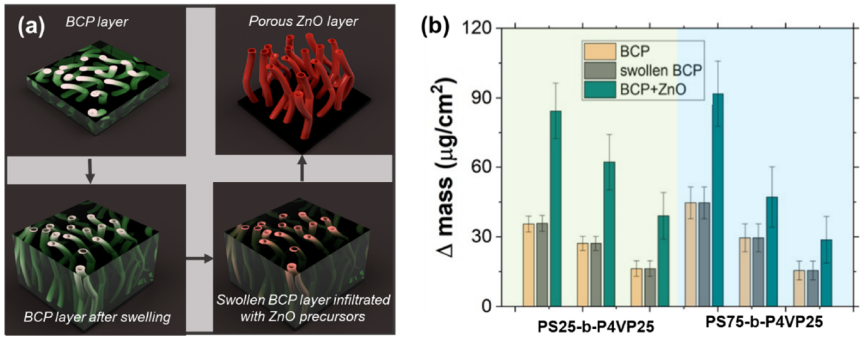

Figure 1. (a) Schematic of the swelling-assisted SIS process enabling deposition of nanoporous ZnO films. (b) QCM data demonstrating the degree of the infiltration of the different BCP templates after the swelling step. The thicknesses of the films were 330, 260, and 150 nm for PS25-*b*-P4VP25 BCP and 420, 280, and 140 nm for PS75-*b*-P4VP25 BCP.

the surface. A vacuum layer of 20 Å was built to avoid interactions between periodic ZnO groups. *K*-point meshes were set up as 3 × 3 × 1 grids.

The potential for the ZnO affinity to ethanol was evaluated by calculating the adsorption energy of surface species during the different steps of the chemical reactions. The adsorption energy is defined as:

$$E_{ads} = E_{total} - E_{surface} - E_{species} \quad (2)$$

where E_{total} represents the total energy of adsorbed species on the ZnO surface, $E_{surface}$ is the energy of the ZnO surface before the reaction step, and $E_{species}$ is the energy of species in the gas phase. The resulting from the VASP calculations changes in the structure of the ethanol molecules adsorbed on the ZnO surface were visualized using the VESTA software.

3. RESULTS AND DISCUSSION

3.1. Swelling-Modified SIS of Porous ZnO Films.

Previous studies demonstrated that the synthesis of ZnO using infiltration of polymers via the SIS approach is possible only with the priming of the polymer template with the alumina layer.[28] The major reason for this is the limited number of reactive sites in the BCP for the attachment of the DEZ molecules even if they diffuse through the nanodomains of the BCP films.[29] However, it was shown that the residual processing solvent can mediate the infiltration of even nonreactive polymers with ZnO precursors.[30] Our previous studies demonstrated improved infiltration of the BCP after the selective swelling in ethanol as a result of the increased number of reactive infiltration sites, thus suggesting the importance of the swelling step prior to the SIS.[31,32] In addition, the swelling increases the porosity, enabling the synthesis of high-surface-area films.[32] As in the case of alumina, we also observed that swelling of the BCP template allowed a significant increase in the infiltration efficiency of the BCP with ZnO precursors. In this study, we explored the swelling of the BCPs with a different contribution of polar domains such as PS25-*b*-P4VP25 and PS75-*b*-P4VP25. Figure 1a depicts the major steps involved in porous ZnO coatings via SIS using swollen BCP templates such as (i) deposition of the BCP layer via spin-coating, (ii) swelling of the deposited BCP in ethanol for 1 h at 75 °C, (iii) infiltration of swollen BCP with ZnO precursors by cycling the exposure of template to DEZ and H_2O, and (iv) formation of all-inorganic porous ZnO by polymer removal. The polymer can be removed by thermal annealing or ozone cleaning.[33] In this study, we implemented ozone cleaning since prepared QCM samples cannot be heated up to 450 °C required for the complete removal of organics.

QCM analysis (Figure 1b) of BCP templates of varied thicknesses spin-coated on the QCM substrates was used to monitor the mass changes introduced during different steps of the synthesis of porous ZnO conformal coatings. In the case of alumina, the SIS infiltration mass increase has been reported to be directly proportional to the mass of P4VP domains in PS-*b*-P4VP.[34] However, in the case of ZnO, the QCM data suggest that the swelling-induced reactive sites are not present in the entire volume of the polar domains since we did not observe a direct correlation between the content of polar domains and mass change in studied PS-*b*-P4VP BCP templates (Figure 1b). Importantly, the swelling step is needed for improving the efficiency of the ZnO infiltration.

To unravel the binding events in the infiltration of the BCPs with ZnO precursors, we performed FTIR analysis of the PS25-*b*-P4VP25 BCP template after swelling and after infiltration relative to the initial BCP film spectrum (Figure 2a). The swelling in pure ethanol increases delta absorbace

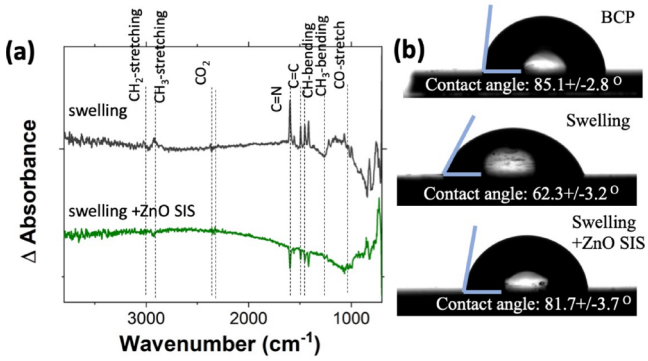

Figure 2. (a) FTIR analysis of the 150 nm thick PS25-*b*-P4VP25 BCP during swelling and infiltration with ZnO processes. The FTIR spectra were normalized to the FTIR spectrum of the as-deposited BCP to highlight the changes of the functional groups initiated by swelling and infiltration processes. (b) Contact angle data demonstrating the wettability of the as-deposited PS25-*b*-P4VP25 BCP, BCP swollen in ethanol for 1 h at 75 °C, and BCP swollen and infiltrated with ZnO precursors (DEZ and H_2O) for five cycles.

because of the CH bending of CH_3 and CH_2 groups at 1580, 1500, 1450, and 1410 cm^{-1}.[35] Analysis of the swollen BCP after the SIS step indicated that swelling creates major sites for infiltration with ZnO precursors. The contact angle measurements (Figure 2b) demonstrate that swelling makes the polymer surface more hydrophilic as evidenced from the

https://doi.org/10.1021/acsami.1c08225
ACS Appl. Mater. Interfaces 2021, 13, 35941−35948

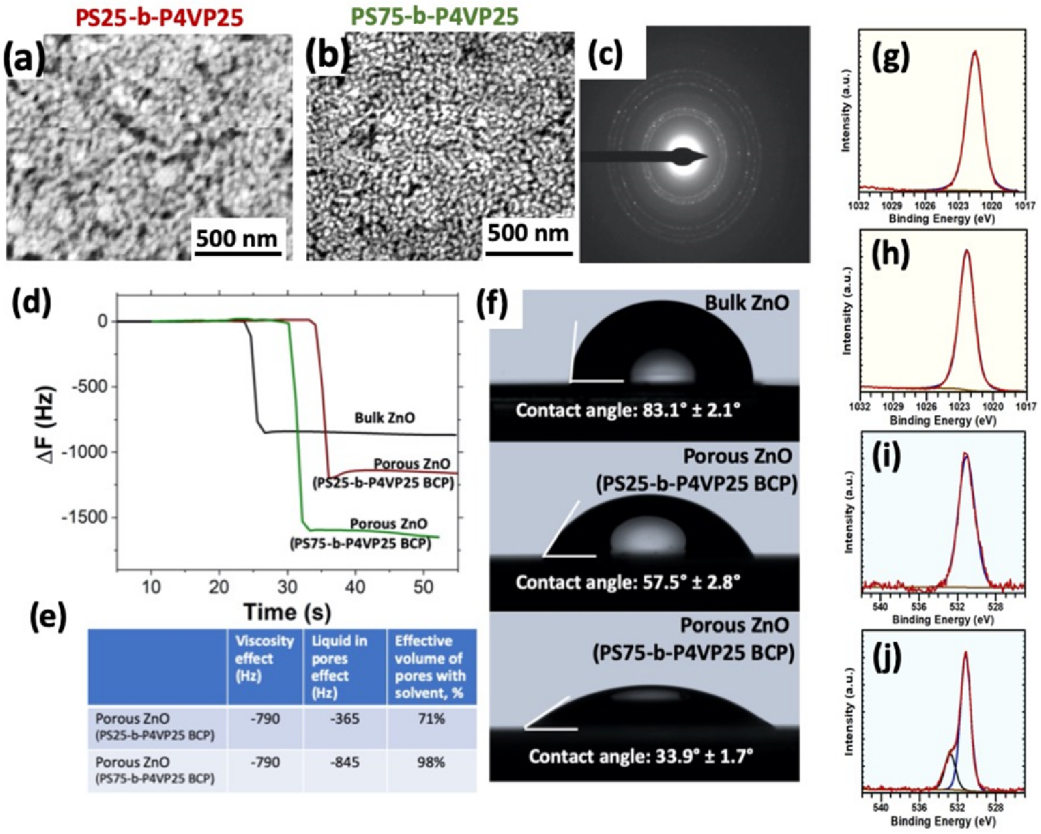

	Viscosity effect (Hz)	Liquid in pores effect (Hz)	Effective volume of pores with solvent, %
Porous ZnO (PS25-b-P4VP25 BCP)	-790	-365	71%
Porous ZnO (PS75-b-P4VP25 BCP)	-790	-845	98%

Figure 3. SEM images of the films grown using (a) 150 nm PS25-*b*-P4VP25 and (b) 140 nm PS75-*b*-P4VP25 BCP templates. Electron diffraction was performed on porous ZnO films synthesized via swelling-assisted SIS (c). Pore accessibility and wetting characteristics of nanoporous ZnO films obtained from 260 nm thick PS25-*b*-P4VP25 BCP and 280 nm thick PS75-*b*-P4VP25 BCP: (d) delta frequency change, upon immersion in water, of the QCMs modified with porous and continuous (bulk) ZnO conformal coatings and (e) estimated amount of water filling the pores. (f) Water contact angle data on the nanoporous ZnO films and bulk ZnO film. XPS analysis of Zn2p and O1s peaks for ALD ZnO (g,h) and SIS ZnO (i,j). The continuous "bulk" ZnO films were obtained via 500 cycles of ALD.

decrease of the contact angle of water droplets deposited at swollen BCP layers as compared to the initial BCP. In turn, infiltration of swollen BCP with ZnO precursors makes the surface more hydrophobic since the contact angle at the interface between the water droplet and infiltrated BCP increases. This observation indirectly confirms that sites capable of binding ZnO precursors were generated during swelling. Such modification of BCP enables the deposition of ZnO without the necessity of priming the polymer template with alumina.

After the successful ZnO infiltration, to create nanoporous ZnO structures (Figure 3), the polymer templates were removed by UV ozone cleaning that previously showed effectiveness in polymer removal.[34] The SEM data indicate the overall uniformity of the porous ZnO coatings (Figure 3a,b) as a result of efficient nucleation and growth of inorganic clusters within the polymer domains that ensure the formation of continuous ZnO materials similarly to various SIS-synthesized structures observed previously.[36] The electron diffraction analysis points out a good crystallinity of the synthesized ZnO coatings (Figure 3c), which is further supported by the XRD analysis (Figure S1). The XRD analysis indicates the estimated size of the crystalline domains to be ∼2 nm.

The accessibility of the pores was analyzed by monitoring the changes in the resonant frequency of the QCM oscillations upon immersing the samples in water (Figure 3d). We observed that the change in the frequency originated from both water trapping in the pores and the effect of the surrounding viscous medium as depicted by eq 3:

$$\Delta f = -f^{3/2}\sqrt{\frac{\rho_L \eta_L}{\pi \rho_q \mu_q}} - \frac{2f^2}{A\sqrt{\rho_q \mu_q}}\Delta m \qquad (3)$$

where ρ_L and η_L are the density and viscosity of the liquid, respectively. In the case when QCM is immersed in water, ρ_L is 0.9982 g/cm^3 and η_L is 0.01 g/(cm s).[37,38] Since the infiltration with inorganic precursors takes place only in polar domains and assuming their full infiltration, we can roughly estimate that the porosities of final ZnO conformal coatings deposited using the PS25-*b*-P4VP25 and PS75-*b*-P4VP25 templates were 50% and ∼70%, respectively. Our QCM experiments indicated that ∼71% and ∼98% of pores were accessible to the solvent. This observation emphasizes the high interconnectivity of the pores in deposited ZnO conformal coatings (Figure 3). These data are in agreement with our previous data on porous alumina conformal coatings indicating that up to 98% of the pore volume is available for solvents and vapors.[20,22]

The XPS data (Figure 3g) reveal that the "bulk" film is characterized only by one symmetric peak at 1020.8 eV that corresponds to Zn atoms in ZnO lattices of the bulk material. Meanwhile, the XPS spectrum of the porous ZnO films has the Zn $2p_{3/2}$ peak shifted to the higher energy values with a maximum at 1022.3 eV, suggesting Zn^{2+} coordination with OH

https://doi.org/10.1021/acsami.1c08225
ACS Appl. Mater. Interfaces 2021, 13, 35941−35948

groups (Figure 3h).[39] The XPS O 1s spectrum of the porous ZnO film exhibits an asymmetric peak that can be fitted by two peaks with maximums at 531.2 and ~532 eV that correspond to O^{2-} and OH^{-} groups, respectively, while the XPS spectrum of "bulk" ZnO has the peak only at 531.2 eV.[40] Therefore, the XPS analysis of porous ZnO films indicates the presence of a significantly higher concentration of OH groups on the surface of SIS ZnO as compared to ZnO prepared via traditional ALD (Figure 3).

To probe the reactivity of ZnO surfaces with ethanol, we performed DFT calculations (Figure 4). In the case of the ZnO surface terminated with OH groups, interaction with ethanol involves two OH groups:[41]

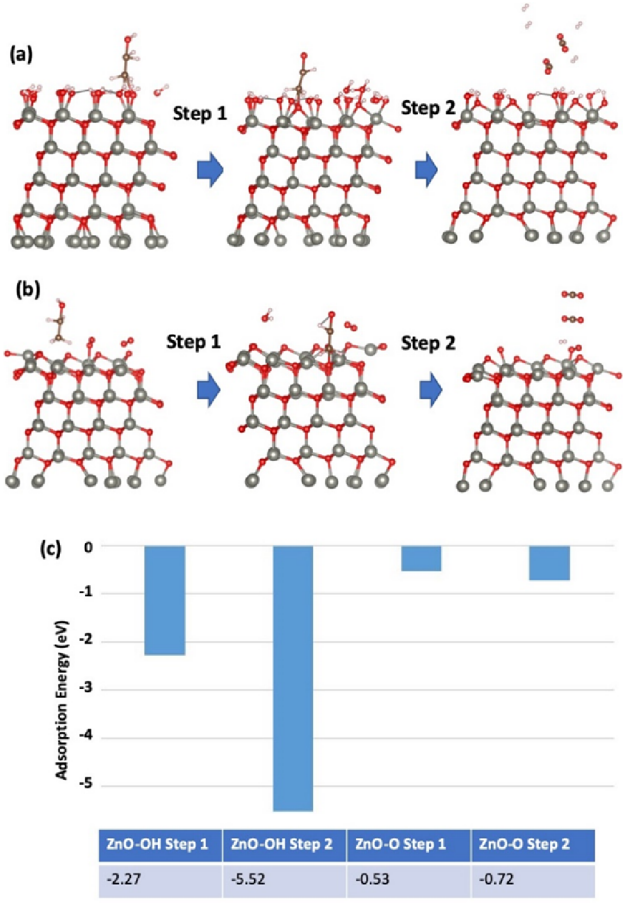

ZnO-OH Step 1	ZnO-OH Step 2	ZnO-O Step 1	ZnO-O Step 2
-2.27	-5.52	-0.53	-0.72

Figure 4. Summary of the DFT calculation results. (a) OH-terminated ZnO surface reacting with ethanol molecules and (b) ZnO surface without OH groups reacting with ethanol molecules. (c) Adsorption energy calculations indicate higher preferability for the reaction with ethanol to proceed in the case of the OH-terminated surface of ZnO.

$$\text{base1} + CH_3CH_2OH = \text{base2} + CH_3CHO + 2H_2O$$

$$CH_3CHO + \text{base2} + H^+ = \text{base3} + 2CO_2 + 4H_2$$

where base 1 is the initial OH-terminated ZnO structure, base 2 is the intermediate ZnO structure with ethanol being reduced to ethanal, and base 3 is the final ZnO structure with surface OH groups being released upon reaction with ethanol.

In contrast, the ZnO surface without OH groups where a single O atom connects to two neighboring Zn atoms interacts with ethanol according to a different reaction path, that is:

$$\text{base1} + CH_3CH_2OH = \text{base2} + CH_3CHO + H_2O$$

$$\text{base2} + CH_3CHO = \text{base3} + 2CO_2 + 3/2H_2$$

where base 1 is the initial O-terminated ZnO structure, base 2 is the intermediate ZnO structure with ethanol being reduced to ethanal, and base 3 is the final ZnO structure with surface OH groups being released upon reaction with ethanol.

Indeed, the DFT calculation results for ZnO terminated with −OH groups (Figure 4) indicated a lower energy barrier for ethanol-induced release of the oxygen restricted depletion layer in the case of the presence of OH groups. Inspired by the presence of high concentrations of OH groups and high interconnectivity of the pores in porous ZnO films, we studied the ability of porous ZnO coatings to sense ethanol since ZnO has been previously reported to demonstrate promising performance for ethanol sensing.

3.2. Ethanol Sensing Using Nanoporous ZnO Films.

An n-type semiconductor, ZnO, is one of the traditional materials used for demonstrating changes in electrical properties as a result of interfacial redox processes.[5] The initial resistance of ZnO, which is an n-type semiconductor, is affected by the adsorption of oxygen from the air that leads to the formation of an electron depletion layer, increasing the surface resistance of ZnO. Upon introducing ethanol, acting as a reducing gas, removal of chemisorbed oxygen leads to the release of conduction band electrons and thus results in resistance decrease. Idriss[42] suggested that in the presence of metal oxide, ethanol undergoes catalytically driven dehydration and dehydrogenation reactions, leading to the formation of gaseous CO_2 and H_2O as the end products that were later detected by a carbon dioxide detector tube installed in the testing chamber by Shankar and Rayappan.[41] It was also suggested that the presence of the hydroxyl groups, chemisorbed as a result of exposing the ZnO material to the humid environment, further promotes the surface reactivity with the ethanol vapor.[41] As the SIS process leads to a higher surface concentration of OH groups, we expect that this can further enhance the sensitivity of the SIS-designed ZnO films to the ethanol vapors.

Here, we combined the QCM analysis[14] with four-probe electrical conductivity monitoring upon exposure of the porous ZnO to ethanol vapors to get insights into structure−property correlations. For this, we designed a vacuum chamber that allowed us to measure the materials' adsorption simultaneously with the changes in the electrical conductivity of the films (Figure 5a). To obtain quantitative estimations of the ethanol-caused changes in the material's properties, we placed two identical samples, one on the QCM and one on the wafer, next to each other to enable the same exposure of both samples. After pumping down the chamber, the samples were exposed to ethanol introduced at a rate of ~3 Torr/min; 1 Torr corresponds to ~1.3×10^3 ppm (Supporting Information).

To probe the sensitivity of the samples to the ethanol exposure, we analysed the changes in the QCM frequency and electrical conductivity of the square samples at room temperature and 90 °C. Figure 5c,d summarizes the results from the tests performed for porous ZnO films synthesized using PS25-*b*-P4VP25 and PS75-*b*-P4VP25 templates at room and at 90 °C that are substantially lower than the temperatures previously reported in other studies that are typically in the 200−400 °C temperature range.[5,6,10,11]

https://doi.org/10.1021/acsami.1c08225
ACS Appl. Mater. Interfaces 2021, 13, 35941−35948

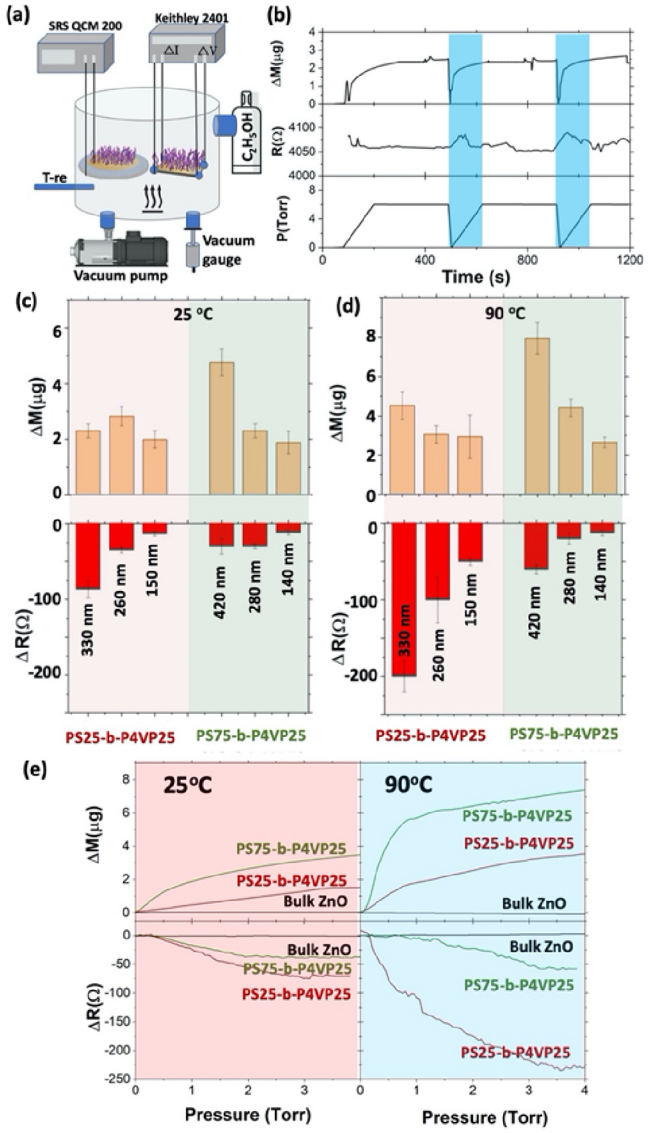

Figure 5. (a) Depiction of the setup used in chemiresistive and QCM tests. (b) Change in adsorption mass and resistance as a function of time upon introducing ethanol for 260 nm thick porous ZnO obtained using PS25-*b*-P4VP25 BCP at room temperature. Simultaneous measurements of QCM mass changes and changes in the electrical conductivity (c,d) of the ZnO films upon introduction of ethanol vapors at 4 Torr and room temperature (c) and at 90 °C (d). The thicknesses for the porous ZnO films are provided in the graphs. (e) Evolution of the mass and resistivity change for ZnO films obtained using 330 and 420 nm PS25-*b*-P4VP25 and PS75-*b*-P4VP25 templates upon their exposure to ethanol vapors.

We further analyze the measured changes in the QCM resonant frequency to characterize the ethanol absorption efficiency of the nanoporous ZnO films. In a simple model, we assume that ethanol molecules attach to the ZnO surface vertically. Ethanol coverage A_E can be presented as:

$$A_E = N \times \pi r^2 \tag{4}$$

where N indicates the number of ethanol molecules adsorbed on ZnO, which can be determined from the mass changes:

$$N = \frac{\Delta m \times N_A}{M_{ethanol}} \tag{5}$$

By combining eqs 4 and 5, we can roughly estimate the surface coverage of the films as:

$$A_E = \frac{\Delta m N_A \pi r^2}{M_{ethanol}} \tag{6}$$

Table 1 summarizes the resulting ethanol surface area coverage of the films at 25 and 90 °C.

Table 1. Summary of the Ethanol Surface Area Coverage of the Films on the QCMs

	PS25-*b*-P4VP25			PS75-*b*-P4VP25		
	330 nm	260 nm	150 nm	420 nm	280 nm	140 nm
25 °C	183 cm^2	230 cm^2	151 cm^2	381 cm^2	167 cm^2	143 cm^2
90 °C	358 cm^2	238 cm^2	230 cm^2	620 cm^2	350 cm^2	207 cm^2

Figure 5e summarizes the changes in the mass and resistance as a function of the introduced ethanol pressure at room temperature and 90 °C. The results suggest that at room temperature QCM immediately responds to the introduced ethanol vapors, while there is a slight delay (~6 s corresponding to ~0.3 Torr) in the electrical changes of the porous ZnO sample. While QCM enables the detection of ethanol even at room temperature, the change in the resistivity of ZnO is rather noisy at room temperature (Figure 5b). However, heating the sample only up to 90 °C significantly stabilizes and increases the chemiresistive response. Interestingly, though QCM demonstrates sensitivity not only to ethanol but also to adsorption of the water vapors (Figure S2), there are no indicative changes in the resistance response of the films exposed to low pressures of water and other gases including acetone and toluene (Figure S3).

Our results suggest very promising sensitivity of the SIS-deposited nanoporous ZnO even at low temperatures, while traditional ZnO films prepared via ALD, sol–gel processing, hydrothermal synthesis, or molecular beam epitaxy[3−6] usually require elevated temperatures to demonstrate a reduction in resistance. For instance, we observe the change in sheet resistance up to 1000 Ω/□ at 90 °C, which is comparable with changes in resistivity previously measured at significantly higher temperatures of 350 °C.[43] We show that while porous ZnO films are working well when detection of both mass and resistivity changes is used to quantify the surface interactions with the reactive medium (ethanol), different strategies for the optimization of the sensing layer are likely to be required for QCM and chemiresistive detection. Thus, QCM seems to benefit from more porous structures, while we observe that the most porous ZnO films used in this study did not demonstrate the most pronounced drop in resistivity. In fact, the chemiresitive response was more pronounced in the case of ZnO films with 50% porosity. The higher temperature (90 °C) increased the response of the porous ZnO coatings to the exposure to ethanol by 37% and 122% when QCM and resistivity measurements were conducted, respectively. Therefore, an increase in the temperature promotes the interactions of the ZnO surface with ethanol molecules. The temperature not only helps to overcome the activation barrier for ethanol conversion but also improves both chemiresistive and adsorption characteristics of the ZnO surface upon exposure to ethanol.

https://doi.org/10.1021/acsami.1c08225
ACS Appl. Mater. Interfaces 2021, 13, 35941−35948

4. CONCLUSIONS

In conclusion, we demonstrated a new synthetic approach for the design of conformal nanoporous ZnO coatings with high control over porosity, thickness, and composition. We want to emphasize that 140−420 nm thick ZnO conformal coatings were synthesized using only five SIS cycles, while the traditional ALD process would require ∼1000 to 4000 cycles for the films with such thicknesses. Though the QCM results indicated low selectivity of ZnO to different vapors, the coatings demonstrated a promising chemiresistive sensitivity to ethanol vapors even at room temperature, which is attributed to the high hydrophilicity of the coatings when OH groups are present on the material surface. DFT calculations further confirmed the lowering of the energy barrier for ZnO depletion layer removal in the reducing atmosphere of ethanol when the surface of ZnO is rich in OH groups. Moreover, the termination of porous ZnO layers with −OH groups easily functionalized with different functional molecules makes them suitable for biomedical applications.[44]

■ ASSOCIATED CONTENT

Supporting Information

The Supporting Information is available free of charge at https://pubs.acs.org/doi/10.1021/acsami.1c08225.

XRD analysis of the sample crystallinity and pressure conversion analysis; Figure S1, XRD analysis of the ZnO samples; Figure S2, QCM analysis of water and ethanol adsorption; and Figure S3, chemiresistive analysis of the ZnO samples upon introduction of different gases and vapors (PDF)

■ AUTHOR INFORMATION

Corresponding Authors

Elena V. Shevchenko − *Center for Nanoscale Materials, Argonne National Laboratory, Lemont, Illinois 60439, United States; Department of Chemistry and James Frank Institute, University of Chicago, Chicago, Illinois 60637, United States;* orcid.org/0000-0002-5565-2060; Email: eshevchenko@ank.gov

Diana Berman − *Materials Science and Engineering Department and Advanced Materials and Manufacturing Processes Institute, University of North Texas, Denton, Texas 76203, United States;* orcid.org/0000-0002-9320-9772; Email: diana.berman@unt.edu

Authors

Daniel Pleshek − *Materials Science and Engineering Department and Advanced Materials and Manufacturing Processes Institute, University of North Texas, Denton, Texas 76203, United States*

John Tran − *Materials Science and Engineering Department and Advanced Materials and Manufacturing Processes Institute, University of North Texas, Denton, Texas 76203, United States*

Yuzhe Li − *Materials Science and Engineering Department and Advanced Materials and Manufacturing Processes Institute, University of North Texas, Denton, Texas 76203, United States*

Asghar Shirani − *Materials Science and Engineering Department and Advanced Materials and Manufacturing Processes Institute, University of North Texas, Denton, Texas 76203, United States*

Complete contact information is available at: https://pubs.acs.org/10.1021/acsami.1c08225

Notes

The authors declare no competing financial interest.

■ ACKNOWLEDGMENTS

The authors thank Dr. Badri Narayanan (University of Louisville) for the useful discussions regarding the DFT results and Michael Talapin (a junior student at Lyons Township High School, District 204) for his help with graphical work. The authors acknowledge the support of this work by the National Science Foundation, Award No. 2045662. This work was performed in part at the University of North Texas' Materials Research Facility. Support from the Advanced Materials and Manufacturing Processes Institute (AMMPI) at the University of North Texas is acknowledged. Work at the Center for Nanoscale Materials was supported by the U.S. Department of Energy, Office of Science, Office of Basic Energy Sciences, under Contract No. DE-AC0206CH-11357.

■ REFERENCES

(1) Tharsika, T.; Thanihaichelvan, M.; Haseeb, A. S. M. A.; Akbar, S. A. Highly Sensitive and Selective Ethanol Sensor Based on ZnO Nanorod on SnO_2 Thin Film Fabricated by Spray Pyrolysis. *Front. Mater.* **2019**, *6*, 122.

(2) Li, S.-M.; Zhang, L.-X.; Zhu, M.-Y.; Ji, G.-J.; Zhao, L.-X.; Yin, J.; Bie, L.-J. Acetone sensing of ZnO nanosheets synthesized using room-temperature precipitation. *Sens. Actuators, B* **2017**, *249*, 611−623.

(3) Ge, C.; Xie, C.; Cai, S. Preparation and gas-sensing properties of Ce-doped ZnO thin-film sensors by dip-coating. *Mater. Sci. Eng., B* **2007**, *137*, 53−58.

(4) Garzella, C.; Comini, E.; Tempesti, E.; Frigeri, C.; Sberveglieri, G. TiO_2 thin films by a novel sol−gel processing for gas sensor applications. *Sens. Actuators, B* **2000**, *68*, 189−196.

(5) Bhati, V. S.; Hojamberdiev, M.; Kumar, M. Enhanced sensing performance of ZnO nanostructures-based gas sensors: A review. *Energy Reports* **2020**, *6*, 46−62.

(6) Liu, Y.; Koep, E.; Liu, M. A highly sensitive and fast-responding SnO_2 sensor fabricated by combustion chemical vapor deposition. *Chem. Mater.* **2005**, *17*, 3997−4000.

(7) Zhu, L.; Zeng, W. Room-temperature gas sensing of ZnO-based gas sensor: A review. *Sens. Actuators, A* **2017**, *267*, 242−261.

(8) Sun, Y.-F.; Liu, S.-B.; Meng, F.-L.; Liu, J.-Y.; Jin, Z.; Kong, L.-T.; Liu, J.-H. Metal oxide nanostructures and their gas sensing properties: A review. *Sensors* **2012**, *12*, 2610−2631.

(9) Xuan, J.; Zhao, G.; Sun, M.; Jia, F.; Wang, X.; Zhou, T.; Yin, G.; Liu, B. Low-temperature operating ZnO-based NO_2 sensors: A review. *RSC Adv.* **2020**, *10*, 39786−39807.

(10) Korir, K. K.; Catellani, A.; Cicero, G. Ethanol Gas Sensing Mechanism in ZnO Nanowires: An ab Initio Study. *J. Phys. Chem. C* **2014**, *118*, 24533−24537.

(11) Piliai, L.; Tomeček, D.; Hruška, M.; Khalakhan, I.; Nováková, J.; Fitl, P.; Yatskiv, R.; Grym, J.; Vorokhta, M.; Matolínová, I.; Vrňata, M. New Insights towards High-Temperature Ethanol-Sensing Mechanism of ZnO-Based Chemiresistors. *Sensors* **2020**, *20*, 5602.

(12) Sinha, M.; Mahapatra, R.; Mondal, M. K.; Krishnamurthy, S.; Ghosh, R. Fast response and low temperature sensing of acetone and ethanol using Al-doped ZnO microrods. *Phys. E (Amsterdam, Neth.)* **2020**, *118*, No. 113868.

(13) Gupta, S. K.; Joshi, A.; Kaur, M. Development of gas sensors using ZnO nanostructures. *J. Chem. Sci.* **2010**, *122*, 57−62.

(14) Xie, J.; Wang, H.; Duan, M. QCM chemical sensor based on ZnO colloid spheres for the alcohols. *Sens. Actuators, B* **2014**, *203*, 239−244.

(15) Ramgir, N.; Datta, N.; Kaur, M.; Kailasaganapathi, S.; Debnath, A. K.; Aswal, D.; Gupta, S. Metal oxide nanowires for chemiresistive gas sensors: Issues, challenges and prospects. *Colloids Surf., A* **2013**, *439*, 101−116.
(16) Srinivasan, P.; Ezhilan, M.; Kulandaisamy, A. J.; Babu, K. J.; Rayappan, J. B. B. Room temperature chemiresistive gas sensors: Challenges and strategies—a mini review. *J. Mater. Sci.:Mater. Electron.* **2019**, *30*, 15825−15847.
(17) Arshak, K.; Moore, E.; Lyons, G.; Harris, J.; Clifford, S. A review of gas sensors employed in electronic nose applications. *Sens. Rev.* **2004**, DOI: 10.1108/02602280410525977.
(18) Shirani, A.; Lee, J.; Berman, D. Thermal stability and gas absorption characteristics of ionic liquid-based solid polymer electrolytes. *J. Chem. Phys.* **2021**, *154*, No. 054902.
(19) Waldman, R. Z.; Mandia, D. J.; Yanguas-Gil, A.; Martinson, A. B.; Elam, J. W.; Darling, S. B. The chemical physics of sequential infiltration synthesis—A thermodynamic and kinetic perspective. *J. Chem. Phys.* **2019**, *151*, No. 190901.
(20) Berman, D.; Shevchenko, E. Design of Functional Composite and All-inorganic Nanostructured Materials via Infiltration of Polymer Templates with Inorganic Precursors. *J. Mater. Chem. C* **2020**, *8*, 10604−10627.
(21) She, Y.; Goodman, E.; Lee, J.; Diroll, B. T.; Cargnello, M.; Shevchenko, E. V.; Berman, D. Block-Copolymer Assisted Synthesis of All Inorganic Highly Porous Heterostructures with Highly Accessible Thermally Stable Functional Centers. *ACS Appl. Mater. Interfaces* **2019**, *11*, 30154−30162.
(22) She, Y.; Lee, J.; Diroll, B. T.; Scharf, T. W.; Shevchenko, E. V.; Berman, D. Accessibility of the pores in highly porous alumina films synthesized via sequential infiltration synthesis. *Nanotechnology* **2018**, *29*, No. 495703.
(23) Illiberi, A.; Roozeboom, F.; Poodt, P. Spatial atomic layer deposition of zinc oxide thin films. *ACS Appl. Mater. Interfaces* **2012**, *4*, 268−272.
(24) Berman, D.; Guha, S.; Lee, B.; Elam, J. W.; Darling, S. B.; Shevchenko, E. V. Sequential Infiltration Synthesis for the Design of Low Refractive Index Surface Coatings with Controllable Thickness. *ACS Nano* **2017**, *11*, 2521−2530.
(25) Lee, J.; Berman, D. Inhibitor or promoter: Insights on the corrosion evolution in a graphene protected surface. *Carbon* **2018**, *126*, 225−231.
(26) Lee, J.; Atmeh, M.; Berman, D. Effect of trapped water on the frictional behavior of graphene oxide layers sliding in water environment. *Carbon* **2017**, *120*, 11−16.
(27) Berman, D.; Krim, J. Impact of oxygen and argon plasma exposure on the roughness of gold film surfaces. *Thin Solid Films* **2012**, *520*, 6201−6206.
(28) Peng, Q.; Tseng, Y.-C.; Darling, S. B.; Elam, J. W. A route to nanoscopic materials via sequential infiltration synthesis on block copolymer templates. *ACS Nano* **2011**, *5*, 4600−4606.
(29) Peng, Q.; Tseng, Y.-C.; Long, Y.; Mane, A. U.; DiDona, S.; Darling, S. B.; Elam, J. W. Effect of nanostructured domains in self-assembled block copolymer films on sequential infiltration synthesis. *Langmuir* **2017**, *33*, 13214−13223.
(30) Ye, X.; Kestell, J.; Kisslinger, K.; Liu, M.; Grubbs, R. B.; Boscoboinik, J. A.; Nam, C.-Y. Effects of Residual Solvent Molecules Facilitating the Infiltration Synthesis of ZnO in a Nonreactive Polymer. *Chem. Mater.* **2017**, *29*, 4535−4545.
(31) Lee, J.; Hasannaeimi, V.; Scharf, T. W.; Berman, D. Mechanical and chemical robustness of the aluminum oxide-infiltrated block copolymer films and the resulting aluminum oxide coatings. *Surf. Coat. Technol.* **2020**, *399*, No. 126204.
(32) She, Y.; Lee, J.; Lee, B.; Diroll, B.; Scharf, T.; Shevchenko, E. V.; Berman, D. Effect of the Micelle Opening in Self-assembled Amphiphilic Block Co-polymer Films on the Infiltration of Inorganic Precursors. *Langmuir* **2019**, *35*, 796−803.
(33) Berman, D.; Sha, Y.; Shevchenko, E. V. Effect of Polymer Removal on the Morphology and Phase of the Nanoparticles in All-Inorganic Heterostructures Synthesized via Two-Step Polymer Infiltration. *Molecules* **2021**, *26*, 679.
(34) She, Y.; Lee, J.; Diroll, B. T.; Lee, B.; Aouadi, S.; Shevchenko, E. V.; Berman, D. Rapid Synthesis of Nanoporous Conformal Coatings via Plasma-Enhanced Sequential Infiltration of a Polymer Template. *ACS Omega* **2017**, *2*, 7812−7819.
(35) Choi, H. W.; Woo, H. J.; Hong, W.; Kim, J. K.; Lee, S. K.; Eum, C. H. Structural modification of poly(methyl methacrylate) by proton irradiation. *Appl. Surf. Sci.* **2001**, *169−170*, 433−437.
(36) He, X.; Waldman, R. Z.; Mandia, D. J.; Jeon, N.; Zaluzec, N. J.; Borkiewicz, O. J.; Ruett, U.; Darling, S. B.; Martinson, A. B.; Tiede, D. M. Resolving the Atomic Structure of Sequential Infiltration Synthesis Derived Inorganic Clusters. *ACS Nano* **2020**, *14*, 14846−14860.
(37) Lee, J.; Kuchibhotla, A.; Banerjee, D.; Berman, D. Silica nanoparticles as copper corrosion inhibitors. *Mater. Res. Express* **2019**, *6*, No. 0850e3.
(38) Jacques, K.; Joy, T.; Shirani, A.; Berman, D. Effect of Water Incorporation on the Lubrication Characteristics of Synthetic Oils. *Tribol. Lett.* **2019**, *67*, 105.
(39) Wang, M.; Jiang, L.; Kim, E. J.; Hahn, S. H. Electronic structure and optical properties of Zn $(OH)_2$: LDA+ U calculations and intense yellow luminescence. *RSC Adv.* **2015**, *5*, 87496−87503.
(40) Kwoka, M.; Kulis-Kapuscinska, A.; Zappa, D.; Comini, E.; Szuber, J. Novel insight on the local surface properties of ZnO nanowires. *Nanotechnology* **2020**, *31*, No. 465705.
(41) Shankar, P.; Rayappan, J. B. B. Room temperature ethanol sensing properties of ZnO nanorods prepared using an electrospinning technique. *J. Mater. Chem. C* **2017**, *5*, 10869−10880.
(42) Idriss, H. Ethanol reactions over the surfaces of noble metal/cerium oxide catalysts. *Platinum Met. Rev.* **2004**, *48*, 105−115.
(43) Suzuki, T. T.; Ohgaki, T.; Adachi, Y.; Sakaguchi, I.; Nakamura, M.; Ohashi, H.; Aimi, A.; Fujimoto, K. Ethanol Gas Sensing by a Zn-Terminated ZnO(0001) Bulk Single-Crystalline Substrate. *ACS Omega* **2020**, *5*, 21104−21112.
(44) Zhang, Y.; Nayak, T. R.; Hong, H.; Cai, W. Biomedical applications of zinc oxide nanomaterials. *Curr. Mol. Med.* **2013**, *13*, 1633−1645.